Observations of internal tidal dynamics Southwest of Malta in the central Mediterranean Sea

Published Version:
Poulain, P.-M., Oddo, P., Pennucci, G., Lewis, C., Sliwka, J., Duda, T.F., et al. (2023). Observations of internal tidal dynamics Southwest of Malta in the central Mediterranean Sea. CONTINENTAL SHELF RESEARCH, 254, 1-16 [10.1016/j.csr.2022.104922].

Availability:
This version is available at: https://hdl.handle.net/11585/915612 since: 2023-02-15

Published:
DOI: http://doi.org/10.1016/j.csr.2022.104922

(Article begins on next page)

Observations of internal tidal dynamics southwest of Malta in the central Mediterranean Sea

Pierre-Marie Poulain[a], Paolo Oddo[a,+], Giuliana Pennucci[a], Craig Lewis[a], Jan Sliwka[a], Timothy Frederick Duda[b] , Aldo Drago[c]

[a]*NATO-STO-CMRE, La Spezia, Italy.*

[b]*WHOI, Woods Hole, Massachusetts, USA.*

[c]*Physical Oceanography Unit, Malta.*

[+]*now at University of Bologna, Bologna, Italy.*

Abstract: Internal tidal dynamics are investigated southeast of Malta in the central Mediterranean using temperature, salinity, and current data from moorings on the shelf, slope, and deep sea. The greatest variability below the mixed surface layer and the sharp thermocline (below 60 m) is at the diurnal K1 tidal frequency, with the signal being significantly enhanced from the deep sea to the shelf and being fortnightly modulated. Harmonic analysis shows that the diurnal vertical displacements at the shelf break can reach an amplitude of 15-25 m at 160 m depth. The corresponding vertical velocities are ~0.1-0.2 cm s^{-1}. Horizontal currents are maximum (10-15 cm s^{-1}) at about the same depth. They rotate clockwise and counterclockwise above and below ~160 m, respectively. The internal K1 tidal signal is interpreted as a northwestward propagating shelf wave with a phase velocity close to 1 m s^{-1} and a wavelength of the order of 100 km. Horizontal and vertical currents at semi-diurnal (M2) frequency are much smaller (less than 2-3 cm $s^{-1}$and ~0.02 cm s^{-1}, respectively).

Keywords: *Mediterranean Sea, internal tide, shelf wave.*

Corresponding author: Pierre-Marie Poulain, NATO-Science and Technology Organization - Centre for Maritime Research and Experimentation (NATO-STO-CMRE), Viale San Bartolomeo 400, La Spezia 19126, Italy. Pierre-Marie.Poulain@cmre.nato.int

1. Introduction

Internal tides are internal gravity waves with tidal frequency. They have been observed in all oceans of the world and studied in detail both theoretically and experimentally as early as the 1970s (Wunsch, 1975). They are particularly pronounced in shallow seas and continental shelf regions where they can have strong effects on the physical and biological marine environment (*e.g.*, Pingree *et al.*, 1986). Most internal tides are generated by the interaction of tides with topography and can, if they are superinertial, propagate far from their point of origin (Ray and Mitchum, 1997). The mixing and dissipation associated with the breaking of internal tides is a key element in the dissipation of tidal energy and the mixing of the ocean in general (St. Laurent and Garrett, 2002).

Tidal sea level variations and associated currents are generally small in the Mediterranean Sea because of its small size and limited direct gravitational forcing. However, Atlantic Ocean tides and boundary forcing at the Strait of Gibraltar generate tidal signals that propagate throughout all sub-basins of the Mediterranean and interact with its complex topography (Pugh, 1987; Tsimplis *et al.*, 1995). As a result, tidal currents reach considerable amplitudes in certain areas such as the eastern Alboran Sea, the Sicily Channel, the northern Adriatic Sea, and the Gulf of Gabès, although sea level variations remain limited to 0.5 m (see Poulain *et al.*, 2018 for an overview and references therein). In particular, the Sicily Channel connecting the Western and Eastern Mediterranean basins is characterized by substantial tidal currents influenced by its complex bottom topography. Current measurements at various locations and depths in the Sicily Channel by Grancini and Michelato (1987) revealed the amplification of the tidal currents on the Sicilian continental shelf with the predominance of the diurnal signal near Malta. Seasonal modulation was observed with the maximum amplitude of diurnal tidal currents in summer (~10 cm s^{-1}). Shipboard Acoustic Doppler Current Profiler (ADCP) data collected by Gasparini *et al*. (2004) showed maximum tidal currents of 20-25 cm $s^{-1}$for the M2 semi-diurnal constituent (period = 12.42 h) and 5-10 cm s^{-1} for the K1 diurnal component (period = 23.93 h) on the Adventure Bank in the western part of the Sicily Channel. Large diurnal currents (~5 cm s^{-1}) were also detected further east over the Maltese Bank. The latter results were obtained with data from high-frequency coastal radars (Cosoli *et al.*, 2015) and drifters (Poulain *et al.*, 2018).

Numerical simulations of the barotropic tides in the Sicily Channel by Molines (1991) and Abdennadher and Boukthir (2006) confirmed the amplification of K1 and M2 currents on the Adventure Bank and of diurnal tidal currents on the Maltese Bank. More recent barotropic models, *e.g.*, the OSU TPXO (Padman and Erofeeva, 2004) and the FES2014 (Carrere *et al.*, 2015) models, showed that southeast of Malta (near the southern edge of the Maltese Bank), sea level variability is essentially semi-diurnal (M2) with an amplitude of approximately 10 cm. In contrast, barotropic currents are mainly diurnal (K1) with a maximum velocity of ~5 cm s^{-1}. The depth-integrated K1 energy flux is from the Ionian Sea (southwestward; Adennadher and Boukthir, 2006).

The literature on internal tides in the Mediterranean Sea is rather scarce. The baroclinic structure of the tidal currents in the Sicily Channel was first observed by Artale *et al*. (1989) by means of temperature records at ten different depths in the water column near the shelf break on Adventure Bank. Using spectral and harmonic analyses, they found that a coastal-trapped wave (CTW) at diurnal period dominates the temperature fluctuations below the surface mixed layer. The peak-to-peak magnitude of the diurnal tide oscillation is ~10 m at the thermocline depth.

Intense diurnal subsurface currents were also observed on the Maltese Bank near Mellieha Bay (northwest of Malta), associated with a vertical oscillation of the thermocline depth spanning an amplitude of about 4 m (Drago, 1995). These diurnal tidal baroclinic currents are believed to be the expression of a CTW that takes the form of an internal Kelvin-like waveform in the deeper sea, away from the shelf break and is accompanied by shelf wave modes propagating over the continental shelf. It is speculated that they are generated at the steep shelf slopes south of the Maltese Islands or to the East over the Maltese escarpment.

The baroclinic nature of the tide was also speculated by Poulain *et al*. (2018) to explain the large variability of the phase of the K1 signals in surface drifter velocities. Numerical simulations (Abdennadher and Boukthir, 2016) have confirmed the presence of internal tides influenced by the complex local bathymetry of the Sicily Channel at semi-diurnal frequency.

Because the Mediterranean Sea is north of 30°N, linear three-dimensional internal waves at diurnal frequencies are subinertial and cannot propagate freely. However, the interaction of barotropic tides with topography can generate two-dimensional internal waves that are trapped by the topographic slope and propagate along this slope as shelf waves. In the Northern Hemisphere, these waves propagate with the coast or shelf to their right (Le Blond and Mysak, 1978; Mysak, 1980). The relative importance of stratification with respect to topographic slope can be measured by the topographic Burger number, S, which is defined as $S = N^2 H^2 / f^2 L^2$, where N is the buoyancy (or Brunt-Vaisala) frequency, H is the ocean depth, f is the inertial frequency, and L is the width of the shelf slope (Huthnance, 1978; Mysak, 1980). A small value of S corresponds to barotropic shelf waves, while a large value means that stratification is important and corresponds to internal Kelvin-type waves (Huthnance, 1978).

In this paper, *in-situ* observations of temperature, salinity, and currents southeast of Malta (eastern part of the Sicily Channel; see geography in Figure 1), collected during the Mediterranean Rapid Environmental Picture 2020 (MREP20) experiment in the fall of 2020 are used to examine local dynamics on scales between weeks and hours, with a focus on tidal signals. The MREP20 data are described in Section 2, along with the methods used to analyze them. The main results are presented in Section 3, including the analysis of the vertical and horizontal structures of the tidal variability. Discussion and conclusions can be found in Section 4.

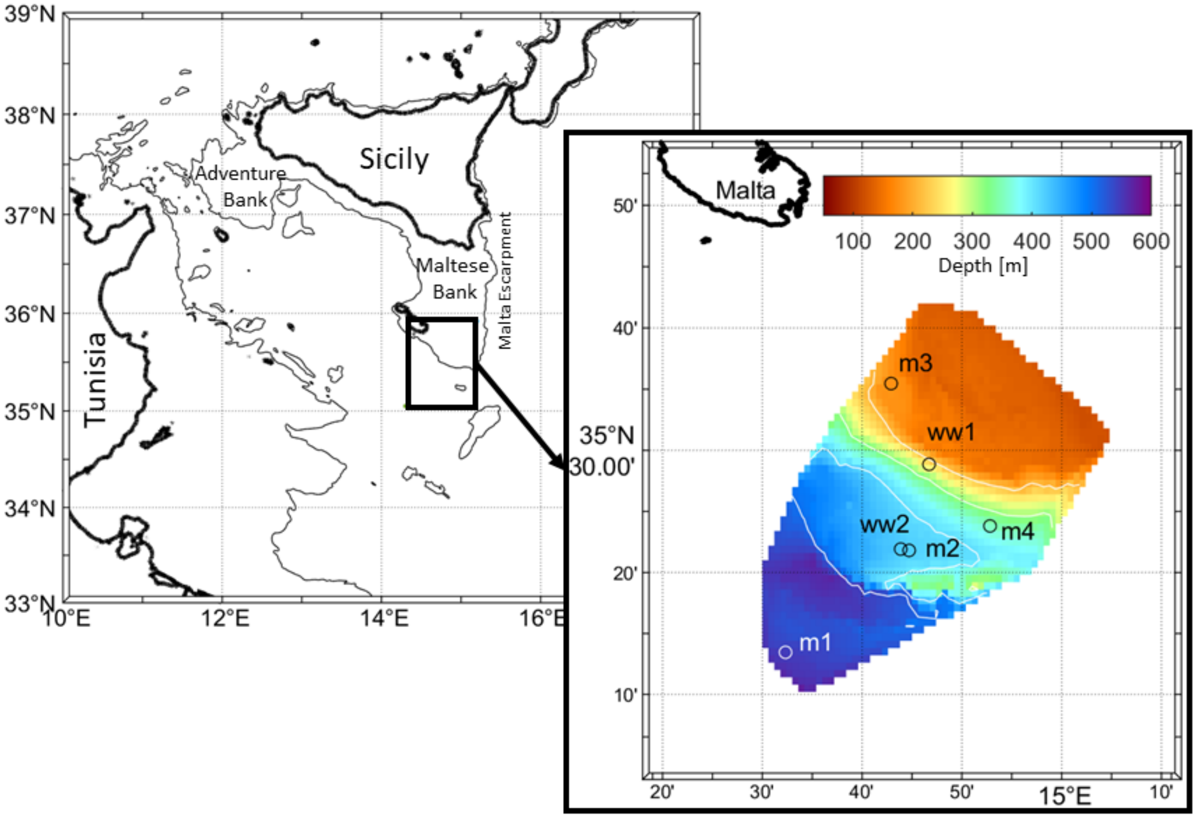

Figure 1: Geography and bathymetry (100 m isobath) of the Sicily Channel area in the Central Mediterranean Sea. Inset: MREP20 study area. Bathymetry as measured by NRV Alliance echo sounder is color-coded and contoured (isobaths at 200, 300, 400 and 500 m). The positions of the moorings are shown with circle symbols.

2. Data and Methods

The data used in this study are part of the MREP20 experiment, whose objective was to investigate oceanographic variability at meso- and submeso-scales (time scales between hours and weeks, spatial scales less than 100 km) in a local Mediterranean environment, and to assess its impact on sound propagation (Poulain and Oddo, 2020). MREP20 was conducted by the NRV Alliance between 27 October and 8 November 2020 in an area southeast of Malta (Figure 1), where modified Atlantic and eastern Mediterranean waters meet with complex dynamics. Equipment deployed included moorings with oceanographic and acoustic instruments, gliders, Lagrangian drifters, and profiling floats. Measurements of temperature, salinity, and currents were also made from the research vessel. In this study, we use only the data from the moored oceanographic instruments, *i.e.*, ADCPs, temperature and salinity sensors, either in a fixed-depth configuration or mechanically profiling along a moored wire.

2.1 Mooring data

The locations of the moorings are shown in Figure 1. One of them (m3) was located on the Maltese Bank. Four moorings (ww1, ww2, m2, and m4) were deployed near the shelf break and slope, and one mooring (m1) was located in deep waters. The maximum slope near ww1 is about 4%. With a sea depth of 500 m, slope width of 20 km, inertial frequency of 0.05 cph and Brunt-Vaisala frequency of 5-15 cph (see below), we obtain a topographic Burger number (S) of ~6-60 for the Maltese slope, confirming the importance of stratification.

Additional details on mooring configuration and technical information on oceanographic instruments are provided in Table 1. Sea-Bird Scientific (SBE) conductivity, temperature, and pressure recorders (SBE 37- SM MicroCAT) and RBR temperature and pressure loggers (RBRduet) were deployed on all moorings except for the moorings with Wirewalkers, i.e. ww1 and ww2. The sampling rate was 10 s and 1 min for the RBR and SBE, respectively. Several Aanderaa single-point current meters (CM) were fitted on m1, m2 and m4.

Wirewalker profilers manufactured by Del Mar Oceanographic were deployed on two moorings (ww1 and ww2) to monitor the upper water column (to ~200 m depth) with high-frequency sampling (with a period as short as 10 min). The Wirewalker moves up and down along a wire that is driven by surface wave motion during descent and uses its own positive buoyancy during ascent

(Pinkel et al., 2011; Poulain et al., 2019). A Wirewalker (ww1) was equipped with an RBRconcerto conductivity-temperature-depth (CTD) and a Nortek Signature 1000 ADCP. CTD data were retrieved inductively from an RBRcervello data controller and transmitted in real time via Iridium. The sampling frequency of the CTD was 8 Hz.

Nortek ADCP data were acquired along four beams at 16 Hz, in 87 cells of 0.25 m for each beam. The sensor was configured in burst mode and data were acquired in beam coordinates (*i.e.*, measurement of radial velocities).The other Wirewalker (ww2) was equipped with an SBE 49 FastCat CTD sensor with a sampling rate of 2 Hz. There was also a WETlabs Eco BB2F to measure chlorophyll concentration, colored dissolved organic matter, and optical backscatter, but these data are not included in this work.

For ww1, upcasts between 200 m and the surface typically lasted ~5 min, while downcast periods varied between 7 min and 4.7 h due to surface wave variability during the experiment (including a lull period on 5-6 November). As a result, the sampling rate at a fixed depth ranged from 10 min to 5 h. The other Wirewalker (ww2) collected data for only a few days, between 30 October and 3 November. During this period, the duration of the upcast was ~6 min and the downcast varied between 8 min and 30 min. This results in a sampling period of 14-26 min at any given depth.

Table 1: Details on the MREP20 moorings.

	Oceanographic Sensors	**Deploy/Recover**	**Lat**	**Lon**	**Water Depth (m)**	**Record length (days)**
m1	ADCP 150 KHz @ 250 m. CM @ 350 and 450 m. SBE @ 30, 120, 230, 340 and 440 m. RBR @ 45, 75, 170 and 300 m.	29-Oct-2020 16:00 UTC 07-Nov-2020 07:00 UTC	35°N13.45’	14°E32.32’	547	8.61
m2	ADCP 300 KHz @ 135 m. CM @ 250 and 350 m. SBE @ 300 m. RBR @ 130, 250 and 350 m.	29-Oct-2020 10:55 UTC 06-Nov-2020 11:00 UTC	35°N21.82’	14°E44.71’	420	7.73
m3	ADCP 300 KHz @ 140 m. SBE @ 45, 50, 115 and 140 m. RBR @ 35, 53, 80, 110, 130, 138 and 153 m.	30-Oct-2020 17:30 UTC 08-Nov-2020 10:00 UTC	35°N35.46’	14°E42.91’	176	8.64
m4	ADCP 150 KHz @ 250 m. CM @ 300 m. SBE @ 45, 115, 165 and 300 m. RBR @ 100, 130, 200, 225, 250, 275 and 340 m.	29-Oct-2020 07:00 UTC 06-Nov-2020 14:40 UTC	35°N23.81’	14°E52.82’	326	8.25
ww1	ADCP 1 MHz. RBR CTD.	27-Oct-2020 11:15 UTC 08-Nov-2020 08:00 UTC	35°N28.86’	14°E46.71’	220	11.89
ww2	SBE CTD.	29-Oct-2020 16:00 UTC 08-Nov-2-2- 06:00 UTC	35°N21.92’	14°E43.87’	424	3.73

The recording period is longest for ww1 (almost 12 days) and shortest for ww2 (almost 4 days). The other moorings have about 8-10 days of data.

2.2 Data analysis methods

The temperature, salinity, and current data were first processed to remove obvious outliers using an automated procedure (with climatological thresholds) and a manual check. The measured temperature and salinity were converted to conservative temperature and absolute salinity, respectively (Feistel, 2012). Pressure at the RBR and SBE sensors was examined. Variations are essentially limited to 0.2 dbar, with exceptional intermittent variations at 1.5 dbar. The effect of these variations on the measurements was found to be negligible, and the assumption of a constant depth for the sensors was confirmed (see details in Appendix A). For the two Wirewalkers, the temperature and salinity data were binned with 0.5 m vertical resolution. Only upcasts were considered. Bi-linear interpolation in depth and time was then performed with 0.5 m and 15 min resolution, respectively.

Vertical displacements of isopycnals with respect to low-pass filtered (3-day mean) isopycnal depths were estimated (see Appendix B for details). This method does not work in the mixed layer and near the maximum profile depth (~200 m), where the density is approximately constant. The high-frequency vertical displacement of isotherms, isohalines, and isopycnals is assumed to be due to the vertical motion of water rather than the horizontal advection of different water masses, given that the vertical gradients of water mass properties are much larger than the horizontal ones. This is confirmed by the little spreading in T-S diagrams below ~ 100 m depth (see Figure 2).

The Nortek ADCP data were processed using a lowered ADCP algorithm based on Visbeck (2002). This algorithm solves the flow estimation problem by converting it into a system of linear equations that can be solved efficiently using least squares. The tilt and compass data are combined with the radial velocities to obtain linear equations that include the components of the ocean current and the velocity of the ADCP, which are the unknowns to be estimated. The main challenge is to constrain the solution to obtain a correct barotropic absolute current. Since the Wirewalker is anchored, it always returns to approximately the same known position after two successive casts. This fact can be used as a constraint, known as the barotropic constraint in Visbeck (2002), which is added to the system of linear equations. This method requires the use of profiling round-trips (up- and down-casts) to estimate the profile of horizontal currents. The vertical resolution of the processed data is 1 m. Estimates of currents were assigned a time equal to the mean time of the two casts. Finally, the data were linearly interpolated at 15-min intervals.

A bandpass filter was applied to the Wirewalker data to extract both the diurnal and semi-diurnal tidal signals. A second-order Butterworth filter with cutoff periods of 6 h and 36 h [-3 db] was used.

Spectral analysis was performed using the multi-taper approach using seven slepian tapers with a time-bandwidth product of 4. Diurnal, semi-diurnal, and inertial signals were found to predominate at the mooring locations on the slope and shelf. However, inertial signals are difficult to separate from diurnal variability because the local inertial period of 20.67 h is close to one day and the time series are short (< 12 days).

We applied standard harmonic analysis with tidal constituents K1 and M2 constituents using the t_tide algorithm (Pawlowicz *et al*., 2002) to the ADCP and temperature, salinity, and density data, and to the isopycnal vertical displacement estimates. A linear trend was removed. For the horizontal currents, the amplitude of the semi-major and semi-minor axes, the rotation coefficient, the ellipse inclination (angle of the northern semi-major axis counterclockwise from east), and the Greenwich phase were calculated. The rotation coefficient describes the direction of rotation and eccentricity of the tidal ellipses. It varies between -1 and 1. Positive and negative values correspond to clockwise (CW) and counterclockwise (CCW) rotation, respectively. For rectilinear tidal currents with tidal reversals, the rotation coefficient is zero. By definition, the Greenwich phase measures the delay between the maximum astronomical force at the Greenwich meridian and the maximum response (largest tidal current) at a given location. Error bars were estimated using bootstrap confidence intervals based on white noise. For scalars such as temperature, the output coefficients are the amplitude and the Greenwich phase. The skill is the percentage of the variance explained by the tidal components compared to the signal variance. Possible contamination of the diurnal variability by inertial motions is limited because the harmonic analysis was mostly performed for time series longer than 6.32 days (Rayleigh criterion). The only exception is ww2. An evaluation of this contamination is provided in Appendix C.

2.3 Barotropic tidal models

Numerical simulations of barotropic tidal currents and sea level elevation in the study area and for the period under consideration were performed using two models: the OSU TPXO (Padman and Erofeeva, 2004) and the FES2014 model (Carrere *et al*., 2015). The simulations proved to be very similar, and the OSU model products were used for comparison with our *in-situ* observations, especially at site ww1.

2.4 Energy flux

The baroclinic energy flux was estimated using the velocity-pressure correlation $\langle \boldsymbol{u}'p' \rangle$ inferred from the Wirewalker density and velocity profiles following Nash *et al.* (2005), Duda and Rainville (2008) and Waterhouse *et al.* (2017). The wave-induced pressure perturbation p' is defined using the hydrostatic equation

$$p'(z,t) = p_{surf}(t) + \int_z^0 \rho' g \, dz \,, \tag{1}$$

where p_{surf} is the surface pressure, g is gravity and ρ' is the density anomaly. The density and velocity anomalies were defined by applying a bandpass filter (6-36 h) on the time series. The baroclinicity condition requires that

$$\int_H^0 p' dz = 0 \text{ and } \int_H^0 u' dz = 0 \,, \tag{2}$$

H being the total water depth. The energy flux F_E is then defined by taking a time average over the wave period or longer interval

$$F_E = \boldsymbol{c_g} E = \langle \boldsymbol{u}'p' \rangle, \tag{3}$$

where E is the wave energy density and $\mathbf{c_g}$ is the group velocity.

3 Results

3.1 Vertical structure measured by the Wirewalkers

The vertical profiles of temperature and salinity measured by the Wirewalkers are shown in the scatter plots of Figure 2. The time averages of the profiles are also depicted. The profiles are characterized by a surface mixed layer with temperature of 22-23 °C and salinity of 38.1-38.4 g kg^{-1}. The Mixed Layer Depth (MLD) is ~50 m, with variations between 40 m and 60 m. A sharp thermocline is located between 50 m and 70 m. Below this depth, there is a weak temperature gradient from 18 °C to 15 °C. The salinity is lowest at 60-70 m depth (38 g kg^{-1}) and corresponds to water of Atlantic origin. Deeper, the salinity increases to values around 39 g kg^{-1}. The potential density anomaly is about 26.1-26.5 kg m^{-3} in the mixed layer and increases to ~29 kg m^{-3} at 200 m depth. The fluctuations around the mean values are much larger for ww1 for all variables. For ww1, the scatter is maximum in the thermocline (40-70 m) for both temperature and density. For ww2, temperature and salinity vary substantially in the surface mixed layer and the thermocline. However, in the surface mixed layer they tend to compensate each other and density variations are small. For both ww1 and ww2 the density scatter shows a minimum near 110 m depth. N^2 was calculated from the individual profiles using a moving mean over 15 m. It was then averaged in time in isopycnal coordinates and plotted versus the mean depth of the isopycnals in Figure 2. It is highest in the thermocline at 60 m, with values near 5 and 6 rad^2 s^{-2} for ww1 and ww2, respectively. Below this depth, it is relatively constant, with a value of about 1-2 rad^2 s^{-2}. In the surface mixed layer and near the bottom, it approaches zero as stratification becomes negligible.

The T-S diagrams for ww1 and ww2 (Figure 2, bottom panels) show that below 100 m depth (*i.e.* for σ_θ larger than 28 kg m^{-3}) the spreading around the mean water mass is much reduced. This fact combined with the substantial variability in water properties below 100 m (at least for ww1) suggest that scatter is probably due to vertical oscillations of the profiles.

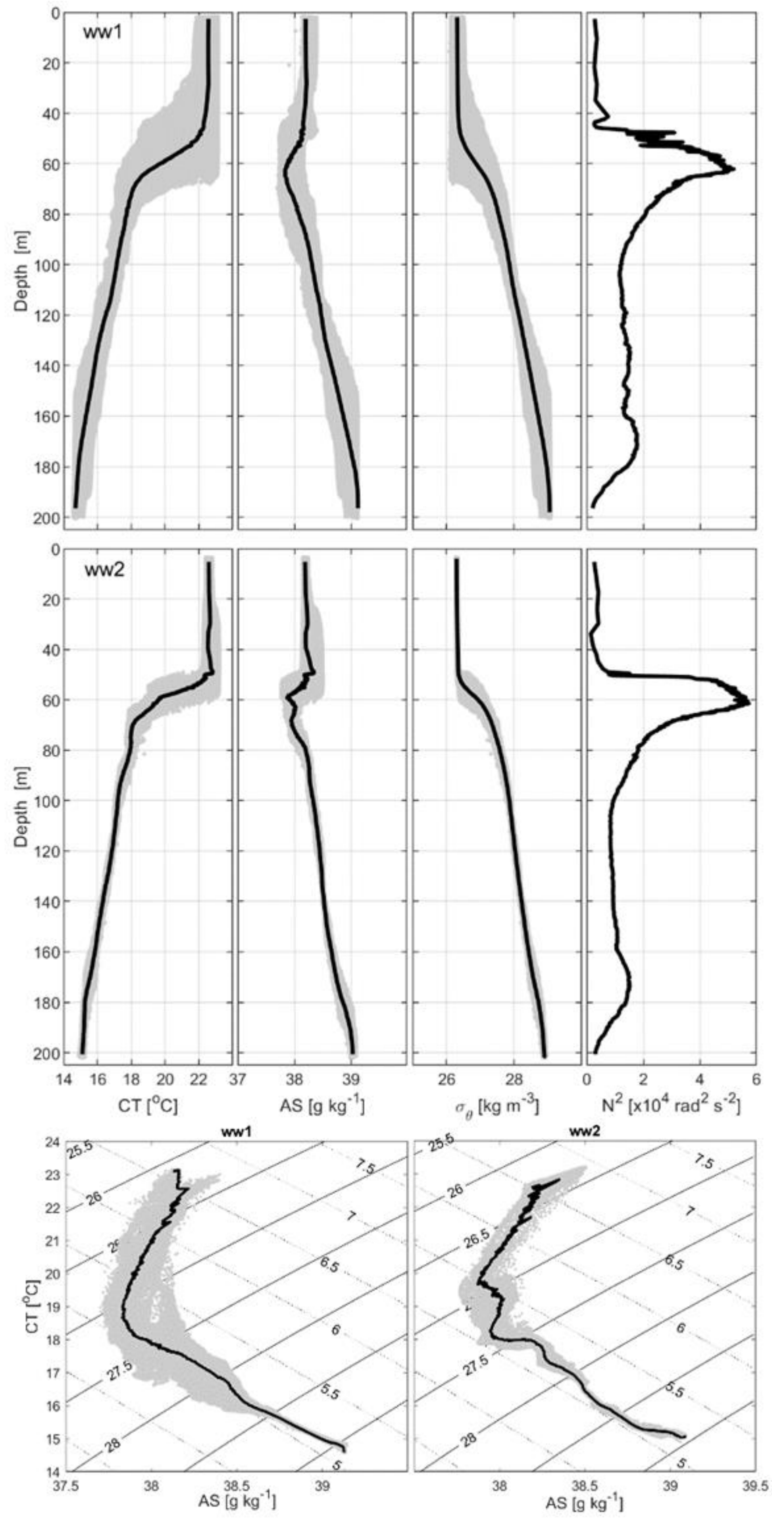

Figure 2: Profiles of conservative temperature (CT), absolute salinity (AS), potential density anomaly (σ_θ) and Brunt-Vaisala frequency squared (N^2) measured by ww1 (top) and ww2 (middle). Individual profiles are in gray, mean profiles in black. Corresponding T-S diagrams with isopycnals and iso-spice curves.

The temporal evolution of thermohaline properties at the Wirewalker sites is shown in Figure 3. For ww1, diurnal variations are ubiquitous in the time series below 100 m. They are most pronounced at the beginning (27-30 October) and toward the end (7-8 November) of the records. In addition, there is a significant shoaling with time of the MLD from 60 m to 40 m. In contrast, deeper isolines (*e.g.,* isopycnals) appear to get deeper with time by about 20-40 m over the entire period. Linear trends were estimated over the entire period.

They show positive (negative) slopes of the isolines above (below) ~110 m depth. Near 110 m depth, the trend is zero, and the variances of temperature, salinity, and density show local minima (discussed earlier and visible in Figure 2). When the above trends are removed from the ww1 time series for temperature and salinity, the correlation between these two variables is positive above 70 m depth. In the mixed layer, they correspond to variations in the warm and saline Mediterranean water. In the thermocline (40-70 m), they are associated with small vertical tidal movements where both vertical temperature and salinity gradients are of the same sign (both temperature and salinity decrease with depth). In contrast, the correlation between temperature and salinity is negative below 120 m, where tidally driven vertical movements of the isolines predominate, and temperature and salinity gradients have opposite signs. For ww2, the diurnal oscillations appear to be much smaller. Temporal trends are not prevalent, partly because the time series are quite short (3.73 days).

Vertical displacements of isopycnals below the mixed surface layer were linearly interpolated to fill data gaps, and low-pass filtered with a 3-hour moving average. They are shown in Figure 4 as a function of depth and time. For ww1, the diurnal signal is striking, with peak-to-peak amplitude reaching 30-50 m at depths close to 160 m.

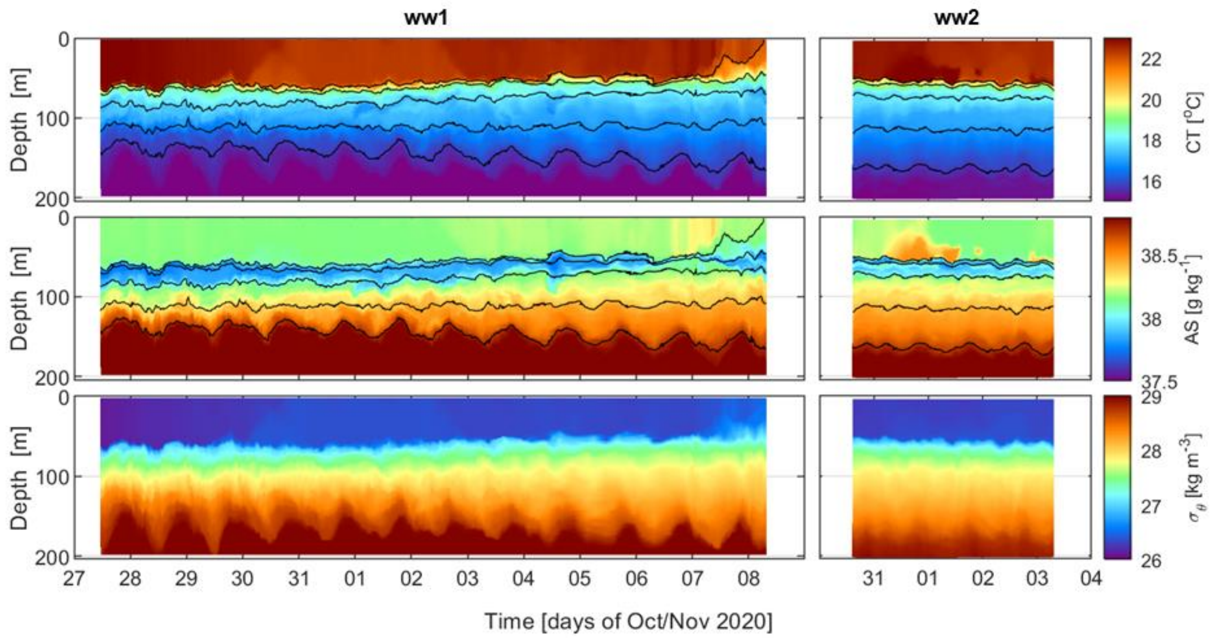

Figure 3: Conservative temperature (CT), absolute salinity (AS) and potential density anomaly (σ_θ) color coded versus depth and time as measured by ww1 (left) and ww2 (right). Isopycnals are overlaid in black on the temperature and salinity plots (contour interval of 0.5 kg m^{-3}).

Note that in the thermocline (near 60 m), the high-frequency vertical displacements are rather small (a few meters), but they can produce large variations in temperature, salinity, and density because their gradients are large there. The vertical velocity of the isopycnals was estimated by finite differences of the low-pass filtered displacements (Figure 4, lower panels). The velocity is obviously 90° out of phase with respect to the displacement. Below 150 m depth, diurnal oscillations with an amplitude of 0.1-0.2 cm s^{-1} (85-170 m day^{-1}) prevail. Bandpass-filtered displacements and velocities better describe the tidal signals, including phase variations with depth and, maximum amplitudes at the beginning and end of the records.

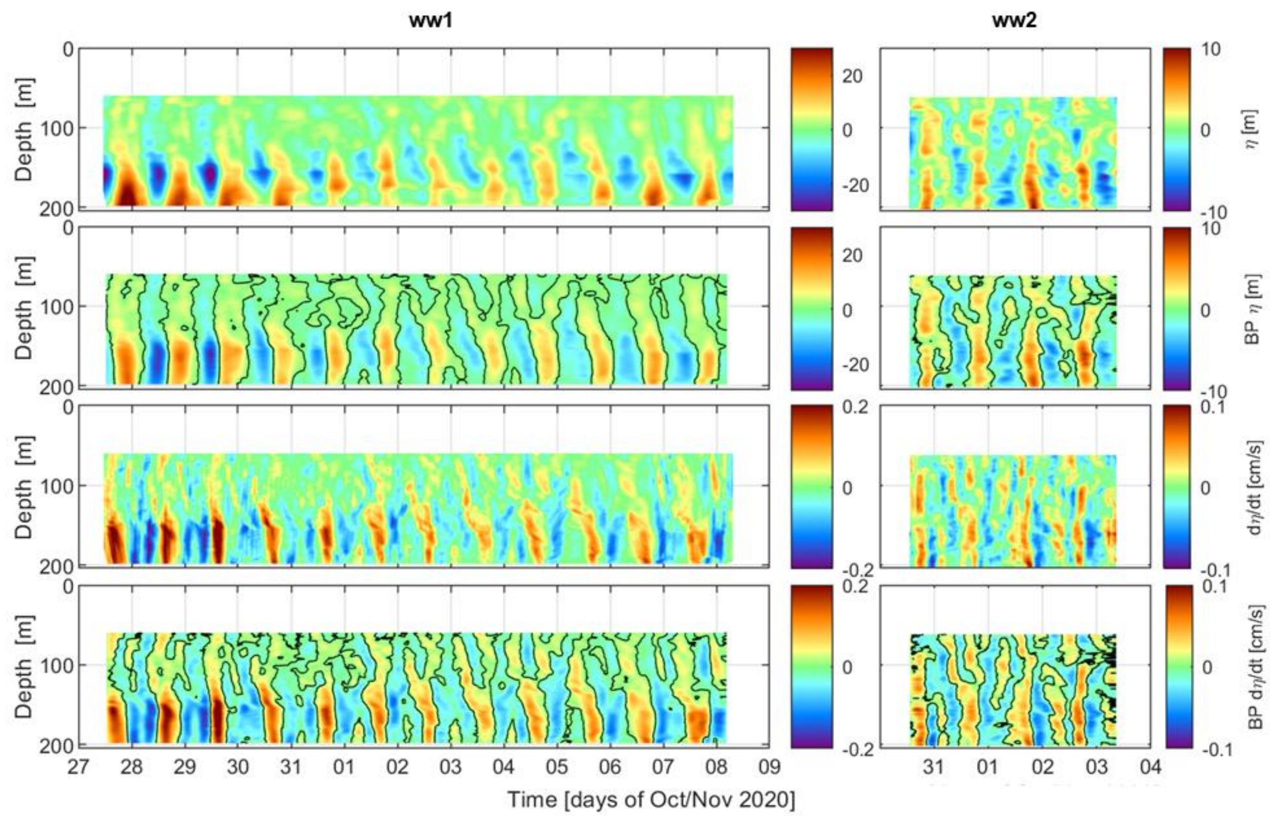

Figure 4: Vertical displacement (*η*; raw and bandpass-filtered, top panels) and vertical speed (d*η*/dt; raw and bandpass-filtered, bottom panels) of the isopycnals color coded versus depth and time as measured by ww1 (left) and ww2 (right). The null isolines are highlighted in the bandpass-filtered data. Note the different color scales for ww1 and ww2.

For ww2, peak-to-peak vertical diurnal displacements are maximum (10-20 m) below 150 m depth. The corresponding velocity reaches 0.05-0.1 cm s^{-1} (40-85 m day^{-1}). The phase appears to be fairly constant with depth.

The time-averaged zonal and meridional ww1 ADCP currents are shown versus depth in Figure 5. In the surface mixed layer (above ~50 m), the currents are essentially northeastward. Below the mixed layer and to a depth of ~150 m, the currents are southeastward and the velocity components approach 10 cm s^{-1}. Below 150 m, currents are weak (< 4 cm s^{-1}) and westward. The variability around the mean profiles is also shown with the amplitude of the semi-major and semi-minor axes of the variance ellipse. The orientation of the major axis of variability is also shown in Figure 5. Above 80 m depth, the velocity variations are mainly zonal with a variance close to 160 cm^2 s^{-2}. There is a subsurface maximum at 140-150 m with a variance of 140 cm^2 s^{-2} in the meridional direction. Below 180 m depth, the velocity variance is less than 30 cm^2 s^{-2} in both directions.

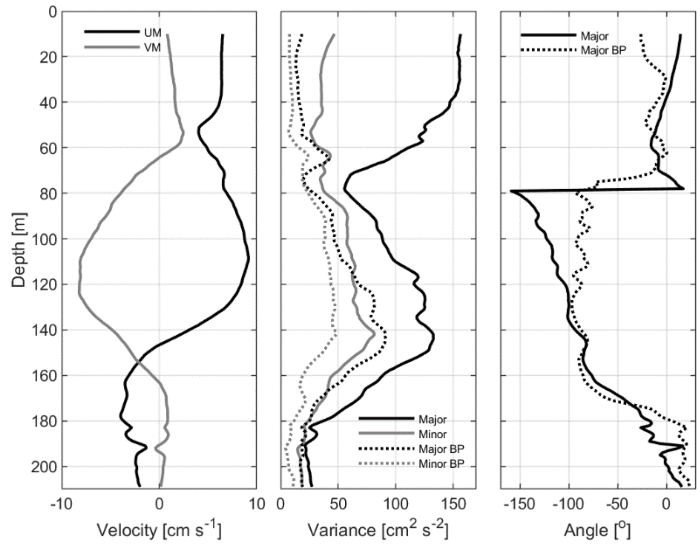

Figure 5: Profiles of mean zonal (black) and meridional (gray) velocity component (left panel), semi-major (solid black) and semi-minor (solid gray) axes of variance ellipse (middle panel) and angle of major axis (right panel; CCW from due East) obtained from the ww1 ADCP data. Dotted curves are the same parameters using the bandpass-filtered data.

The vertical structure of the variance ellipses for the bandpass-filtered horizontal currents (Figure 5) is characterized by two maxima, one at 65 m depth (in the thermocline) and the other at 150 m (with a variance of 90 $cm^2 s^{-2}$). In most cases, the variance along the minor axis is much smaller than along the major axis, indicating a significant eccentricity of the variance ellipses. Near 65 m, the major axis is oriented in the zonal direction. In contrast, between 80 m and 160 m it is essentially oriented in the meridional direction. Below 180 m, the ellipses are more or less oriented in the zonal direction. Given the predominance of the zonal and meridional directions for the major axes of variability, there is no reason to use cross-shelf and along-shelf coordinates, and we have used the standard coordinate system with axes in the east-west (zonal) and north-south (meridional) directions in the analysis presented in this study.

The zonal and meridional components of horizontal velocity measured with the profiling ADCP on ww1 are shown in Figure 6. The variability of the currents is dominated by diurnal signals, especially at depth near 150 m with a peak-to-peak amplitude of ~30 cm s^{-1}. In addition, there is a discontinuity near the base of the mixed layer (40-60 m). In the zonal direction, the currents below 150 m appear to be out of phase compared to those above this depth. In contrast, variations in meridional currents are more uniform (or barotropic) with depth.

When a bandpass filter is applied to the records to emphasize the tidal signals, the diurnal variability becomes even more apparent. As noted earlier for the vertical deflections of the isopycnals, the oscillations are more pronounced at the beginning and end of the sampling period. There is also a significant downward propagation of phase. Near 150 m depth, the zonal currents appear in phase (at 150 m) or out of phase (at 180 m) with respect to the vertical displacements, while the meridional currents are approximately in quadrature with respect to the displacements for all depths below 100 m.

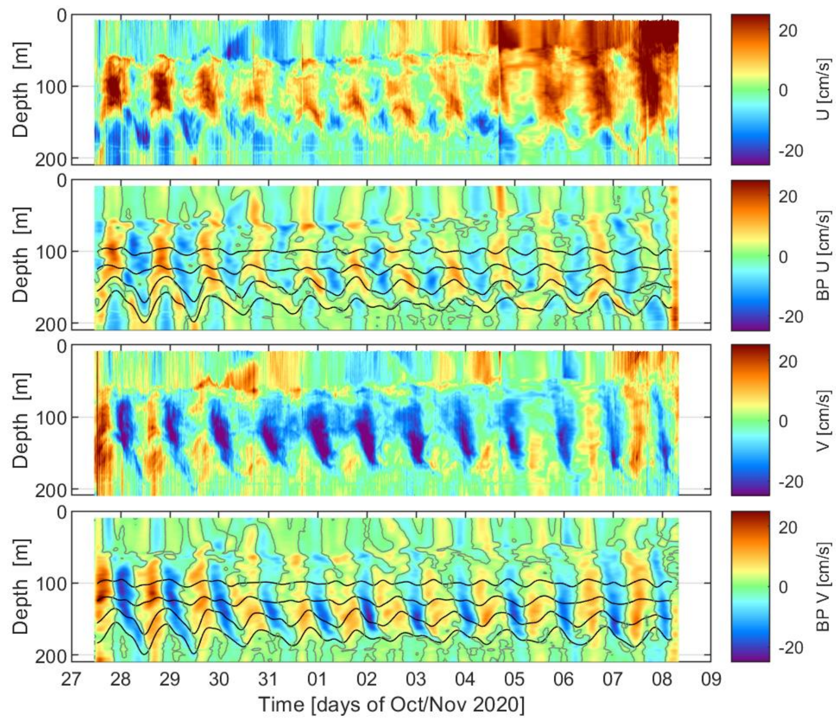

Figure 6: Unfiltered and bandpass-filtered zonal (U; top) and meridional (V; bottom) components of velocity color coded versus depth and time as measured by the ADCP on ww1 between 27 October and 8 November. The null isolines are highlighted in the bandpass-filtered panels. The bandpass-filtered vertical displacements around 100, 125, 150 and 175 m are also superimposed with black curves.

We can combine the density and velocity data collected by ww1 to estimate the horizontal baroclinic energy flux of the prevailing waves using equations 1 to 3. The instantaneous flux versus time and depth is shown in Figure 7, along with its temporal mean and depth-integrated values. Instantaneous values are significant with strong semi-diurnal variations near the bottom as the K1 baroclinic pressure and velocity anomalies are in phase and their product oscillates at twice the K1 period. The mean flux is small (less than 1 W m^{-2}) above 140-160 m. In contrast, near the bottom between 170 and 200 m, values reach -4 and 2 W m^{-2} in the zonal and meridional directions, respectively. Thus, the energy flux of the bottom-intensified K1 internal tide is towards the west-northwest direction. The depth-integrated flux reaches ~1 KW m^{-2} on 27-28 October when the diurnal deflections of the isopycnals are maximum.

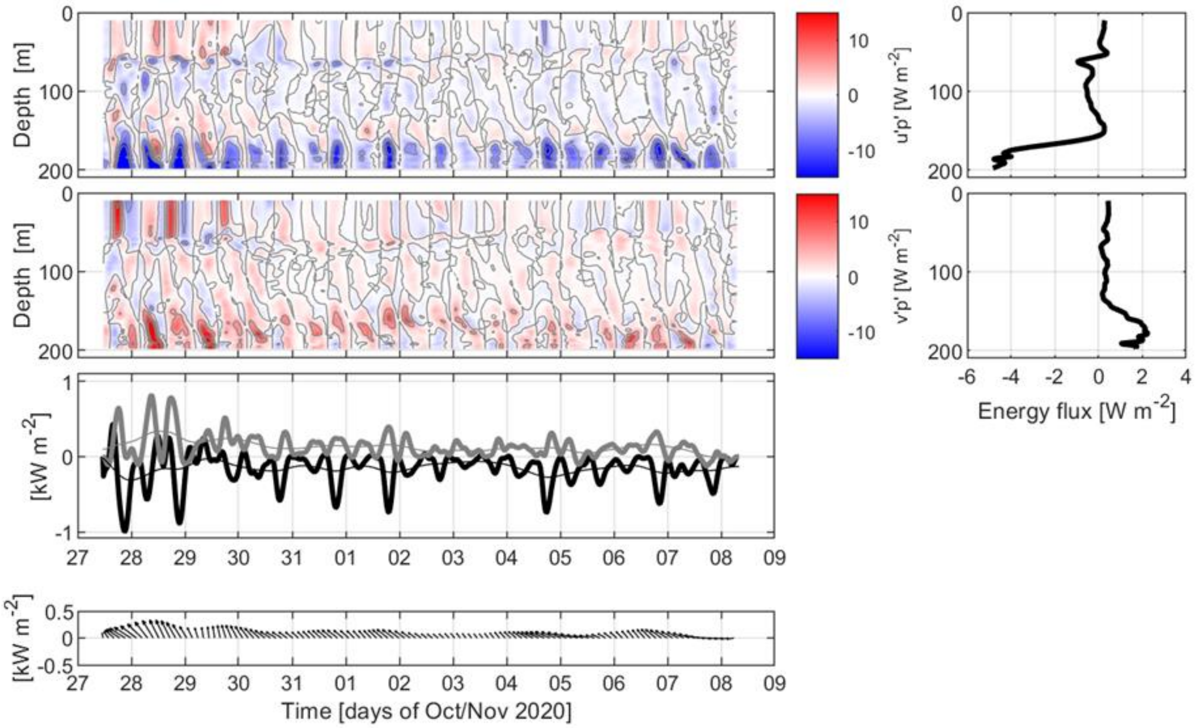

Figure 7: Instantaneous zonal (*u'p'*) and meridional (*v'p'*) baroclinic energy fluxes estimated from the ww1 bandpass filtered data, along with time averaged (right panels). Vertically integrated zonal (black) and meridional (gray) fluxes (middle panel) and corresponding lowpass-filtered energy flux vectors (bottom panel).

Power spectra and power rotary spectra were calculated for all the observed parameters (temperature, salinity, isopycnal displacement, currents). An example is shown in Figure 8 for the depth-averaged currents measured with the ADCP on ww1. Signals with diurnal, semi-diurnal, and near-inertial frequencies in the CW sense of rotation predominate. As mentioned above, given the short time series, the spectral analysis is not suitable to distinguish between diurnal and inertial frequencies. The dominance of diurnal and semi-diurnal tidal variability prompted us to perform a harmonic analysis instead of spectra.

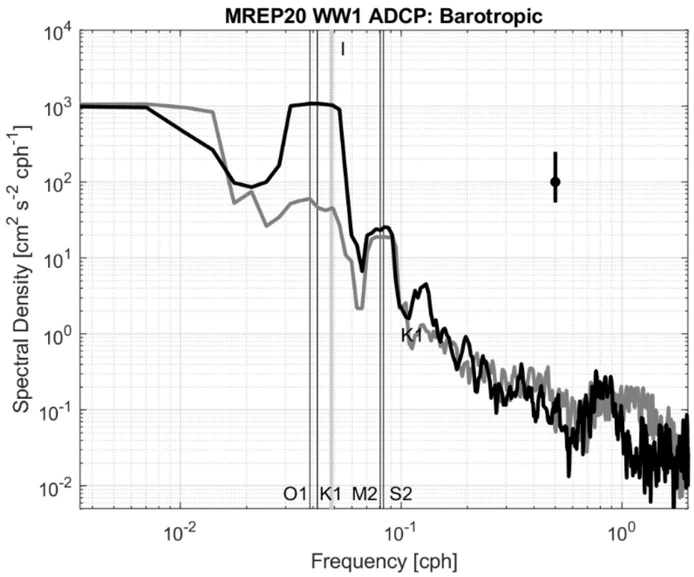

Figure 8: Power rotary spectrum for the depth-averaged (barotropic) currents using the ww1 ADCP data: CW (black) and CCW (gray) components. The 95% confidence interval is indicated. Tidal (O1, K1, M2 and S2) and inertial (I) frequencies are shown as vertical lines.

Since ww1 covers almost the entire water column, the depth-averaged barotropic currents can be estimated and can be compared to the outputs of barotropic tidal models.The depth-averaged and bandpass-filtered currents measured by ww1 are shown in Figure 9 along with the simulations of the OSU TPXO numerical model. The model suggests that the sea level height is mainly semi-diurnal with a maximum amplitude of ~10 cm on 31 October (spring tide). Also, modeled barotropic currents are primarily diurnal, but are significantly underestimated compared to our observations. A better approximate match is obtained for phase. Despite the difference in amplitude, both ww1 and the model show a fortnightly oscillation with minimum currents on 31 October and maximum currents on 7 November.

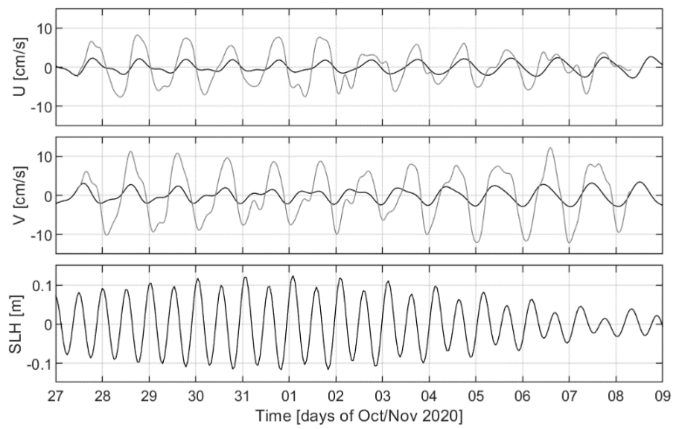

Figure 9: Depth-averaged and low-pass filtered zonal (U) and meridional (V) velocities measured by the ADCP on ww1 (gray lines). Barotropic velocities and sea level height (SLH) predicted by the OSU TPX0 tide model at the ww1 location (black lines).

To analyze the tidal signals from the data collected by the Wirewalkers in more detail, we performed a harmonic analysis using only the diurnal (K1) and semi-diurnal (M2) components.

The results for ww1 are shown in Figure 10 for temperature, salinity, and potential density anomaly. For all scalar variables, the K1 component is largest at 160-170 m depth, where the harmonic analysis tidal model (K1 + M2) explains 60-80% of the total variability. At this depth, the amplitude in temperature, salinity, and potential density is 0.31 °C, 0.13 g kg^{-1}, and 0.17 kg m^{-3}, respectively. For the semi-diurnal tidal band, there is also a relative local maximum at 170 m depth, but with much lower amplitude. For both the K1 and M2 frequencies, temperature variations (and to some extent density) also have a maximum at the MLD near 60 m with an amplitude greater than 0.4 °C for K1 and close to 0.2 °C for M2. As noted above, temperature and salinity vary in phase above 120 m depth and are essentially out of phase below this depth, where the vertical gradients of these properties have opposite signs. The potential density anomaly is in phase with salinity. For ww2, maxima of the semi-diurnal and diurnal amplitudes for temperature, salinity, and density are found near 60 m depth (not shown). They are as large as those of ww1. This is mainly due to the stronger vertical gradients at this location.

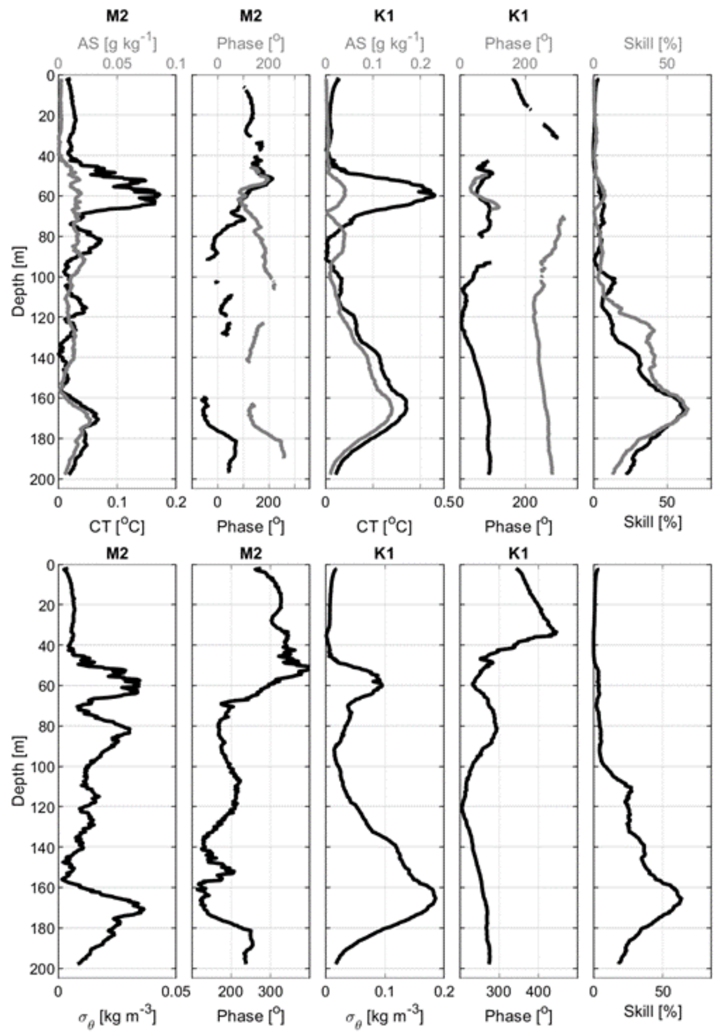

Figure 10: Top: Results of the harmonic analysis for the ww1 conservative temperature (CT, black) and absolute salinity (AS, gray) versus depth. Amplitude and Greenwich phase of the K1 and M2 tidal constituents. Percentage of variance explained by the tides (skill). Phase is only shown for temperature and salinity amplitude larger than 0.02 °C and 0.01 g kg^{-1}, respectively. Bottom: Same for potential density anomaly (σ_θ).

Harmonic analysis was also applied to the vertical isopycnal displacement and corresponding vertical velocity (Figure 11). For ww1, K1 dominates near 160-170 m depth with amplitudes near 13 m, velocities near 0.1 cm s^{-1} and an explained variance (skill) of 60-80%. There is a slight increase in phase with depth, between 120 m and 160 m. By definition, displacement and velocity are 90° out of phase. For M2, vertical displacements are limited to 1.5 m and vertical velocity is less than 0.02 cm s^{-1}. Two maxima are found at 95 m and 170 m. For the maximum at 95 m, the phase increases with depth. At 170 m, there is no significant phase variation. For ww2, the vertical displacements K1 and M2 are limited to 3 m and 2 m, respectively, and the amplitudes generally increase with depth. The phase is fairly constant below 140 m, while above this depth it decreases with depth for M2.

Let us now consider the horizontal currents measured at ww1. Since the diurnal signals predominate, an analysis is presented only for the tidal component K1. The harmonic analysis was performed separately on the zonal and meridional velocity components (Figure 12, left panel) and also on the velocity treated as a complex value (see later). For both components, the K1 amplitude is maximum below 120 m depth with values close to 10 cm s^{-1}. Moreover, the zonal amplitude has a minimum at 160-170 m, corresponding to a drastic phase change of about 180°.

For ww1, the depth-averaged barotropic currents can be estimated and removed from the ADCP velocities to estimate the baroclinic structure of the horizontal currents. The results of the harmonic analysis applied to the baroclinic ww1 currents are shown in the right panel of Figure 12. The baroclinic K1 currents are slightly reduced compared to the previous results, reaching their maximum (no more than 8 cm s^{-1}) below 120 m depth. However, for the zonal component, the local depth minimum and the phase change have shifted to ~155 m. The maximum of the zonal currents is near the bottom. The phase generally increases with depth for both velocity components, indicating upward energy propagation.

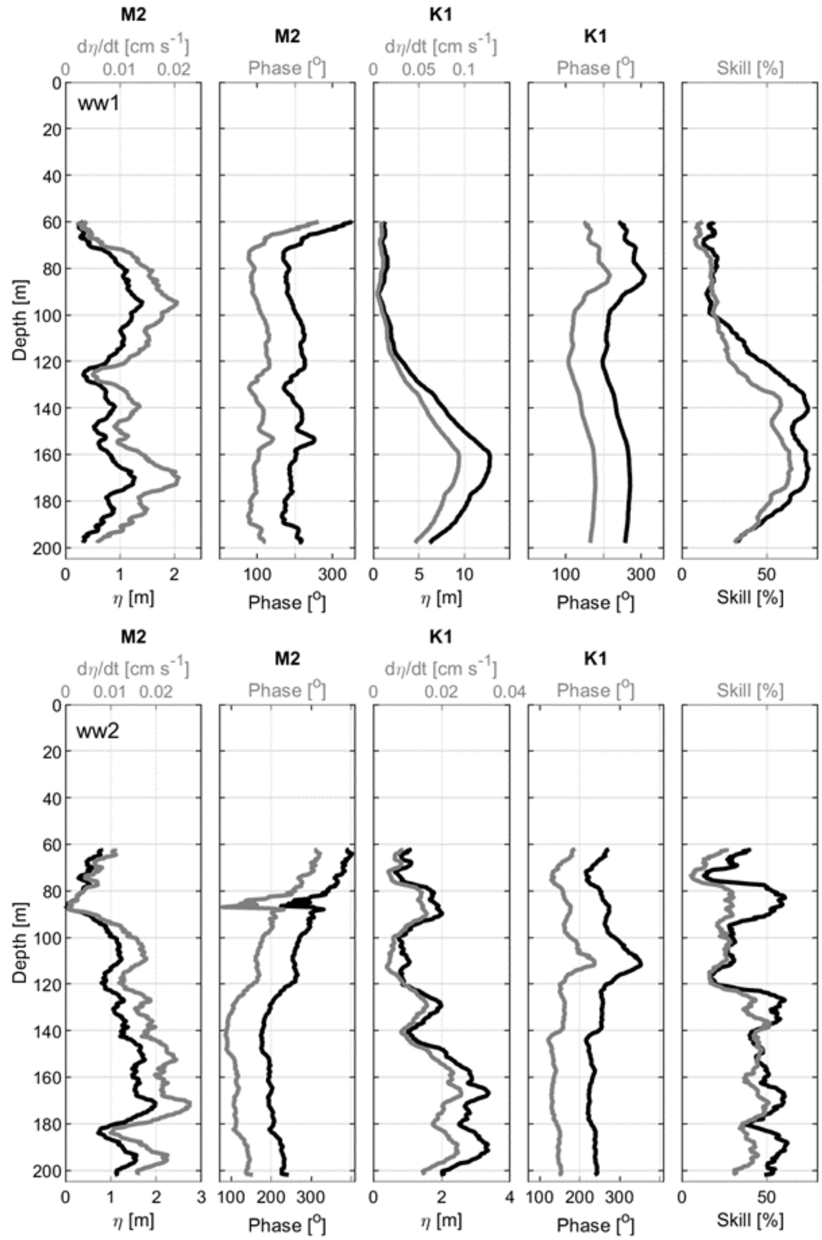

Figure 11: Results of the harmonic analysis (amplitudes, phases and skill) for vertical displacement (*η*; black) and speed (d*η*/dt; gray) of isopycnals: ww1 (top) and ww2 (bottom).

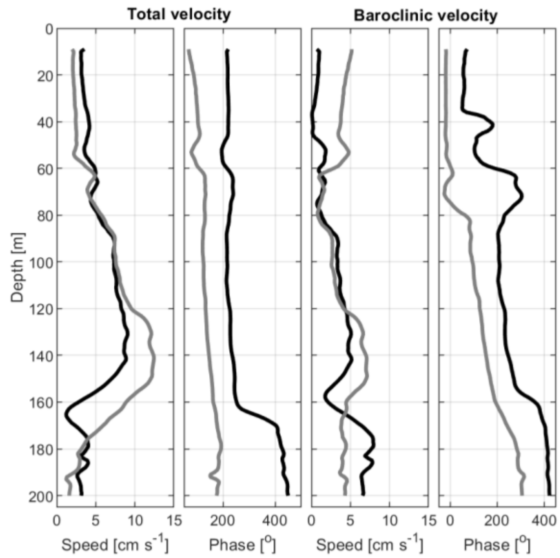

Figure 12: Results of the harmonic analysis for the zonal (black) and meridional (gray) diurnal components of ww1 ADCP velocities: total velocity (left) and baroclinic component (right).

Harmonic analysis was also applied to the two-dimensional ww1 ADCP currents, which are considered as complex values. The results for K1 are shown in Figure 13 for the total and baroclinic velocities. Amplitudes are maximum between 130 m and 150 m, with the semi-major axis reaching 13 cm s^{-1}. At 160-170 m depth, the semi-minor axis is nearly zero and the inclination is ~90°, *i.e.*, the tidal currents are rectilinear in the meridional direction. At the same depth, the rotation coefficient changes sign. Therefore, the elliptical tidal motion changes from CW (top) to CCW (bottom).

As before, the phase and angle of the currents at Greenwich phase zero increase slightly with depth. The baroclinic structure is characterized by K1 currents greater than 5 cm s^{-1} below 120 m depth, with a maximum near the bottom. The semi-major axis is near zero at 160-170 m, but this time the baroclinic currents turn in the same CW direction above and below this depth. A minimum baroclinic signal occurs at 70 m depth. The phase and angle of the currents at Greenwich phase zero increase significantly with depth.

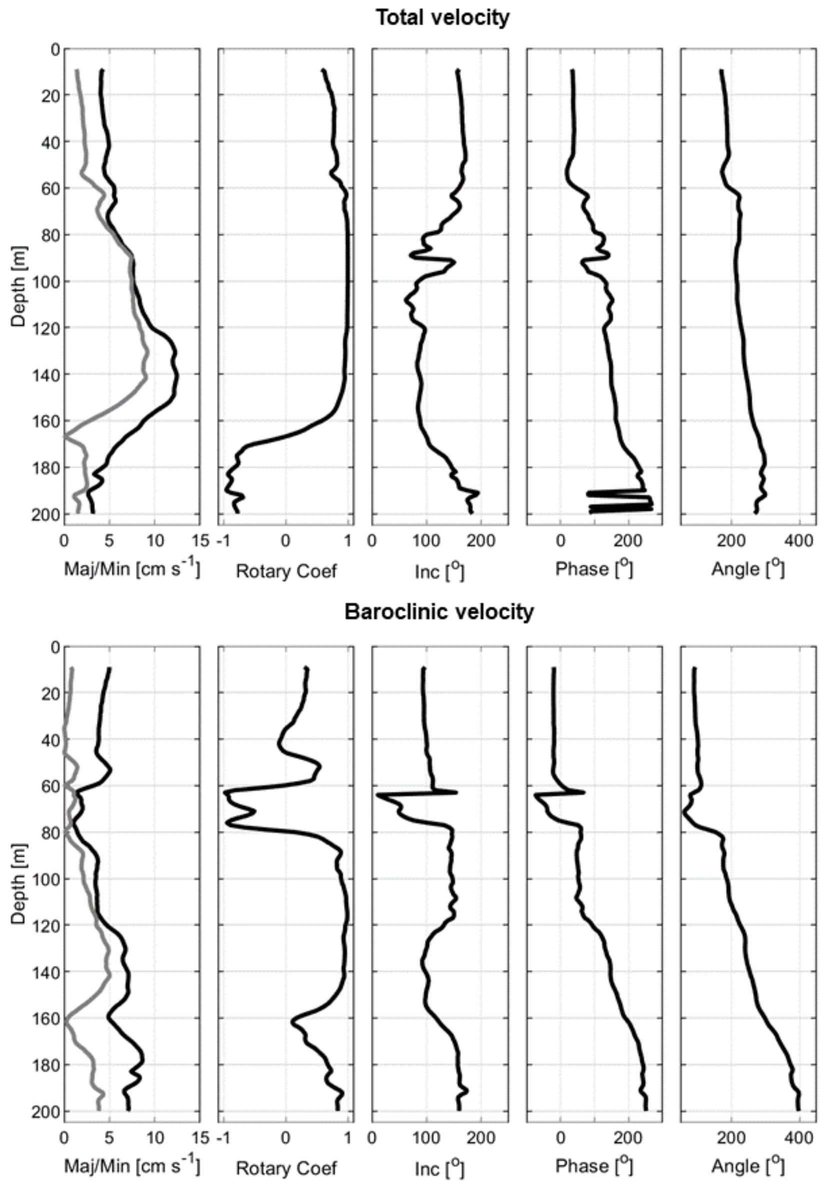

Figure 13: Results of the harmonic analysis applied to the currents (treated as complex values) measured by the ADCP on ww1. Vertical profiles of the K1 parameters: amplitude of major (black) and minor (minor) semi-axes, rotary coefficient, ellipse inclination, Greenwich phase and angle of the velocity vector at zero Greenwich phase. Total velocity (top) and baroclinic component (bottom).

The above results can be illustrated with tidal ellipses (Figure 14) drawn at selected depths (every 20 m). The barotropic ellipse is also shown. It rotates in the CW direction and has a semi-major (semi-minor) axis with an amplitude of 5.6 (4.1) cm s^{-1}, an inclination of 72°, and a phase of 152°. The direction of barotropic flow at zero Greenwich phase is to the southwest. Note that because of the difference in phase, the total ellipse can be smaller, and it can rotate in the opposite direction, with respect to the barotropic and baroclinic counterparts. This is the case near the bottom below 160 m

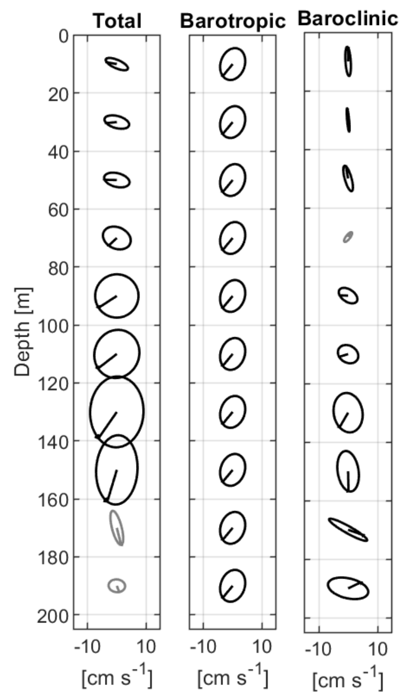

Figure 14: K1 tidal ellipses at selected depths for the total, barotropic and baroclinic currents measured by the ww1 ADCP. CW and CCW rotations are indicated in black and gray, respectively. The line in each ellipse represents the currents at the same time (zero Greenwich phase).

3.2 Horizontal description

We now focus our attention on the horizontal structure of the diurnal tidal dynamics. Since temperature is the most commonly measured parameter at all moorings (with RBR and SBE sensors), we primarily use it to examine amplitude and phase variations at all the mooring locations. The time series of temperature between 153 m and 176 m are shown in Figure 15 (top). In addition to some offsets between the mean temperatures (up to 1 °C), the oscillations with diurnal periods vary significantly with a maximum amplitude close to 0.5 °C for ww1 and m3. In contrast, the amplitudes for m1, m2, and m4 are less than ~0.2 °C. The least squares fit of the tidal component K1 to the above temperature records is also shown in Figure 15 (bottom). The amplitude and phase of the tidal predictions are listed in Table 2. The maximum K1 amplitude for ww1 and m3 is 0.3 °C. For m1, the temperature variations are barely significant (amplitude less than 0.02 °C).

If we exclude moorings m1 and m2, we can see that the internal tide of K1 propagates toward the northwest. For a more precise quantification, we can calculate the phase differences between ww1 and m4, and between m3 and ww1 and estimate the phase velocity and wavelength from these values (see Table 3). The phase velocity is essentially 1 m s^{-1} and the wavelength is between 70 and 110 km.

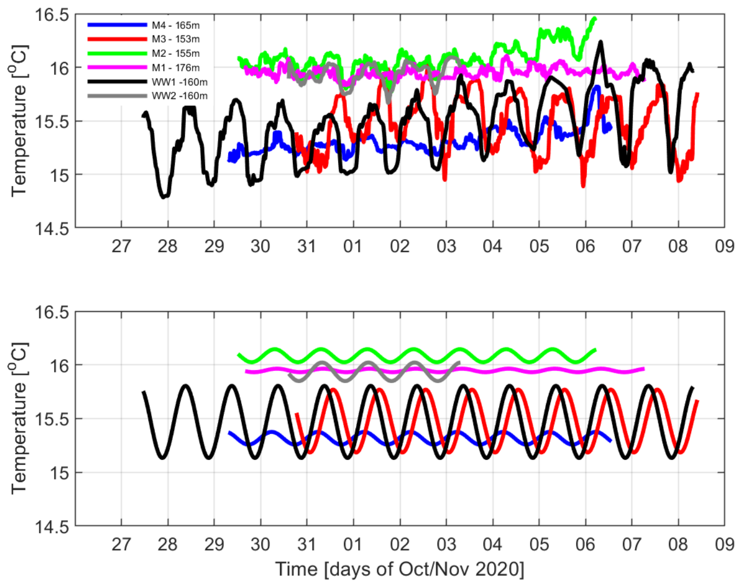

Figure 7: Top: Temperature versus time as measured at all the mooring sites (between 153 and 176 m). Bottom: Corresponding tidal predictions (K1 constituent plus temporal mean).

Table 2: Results of the harmonic analysis using the K1 tidal constituent, applied to the temperature records at all mooring sites between 153 m and 176 m depth.

Mooring	Amplitude [°C]	Phase [°]
ww1 (160 m)	0.33±0.01	76±2
ww2 (160 m)	0.08±0.01	60±7
m1 (176 m)	0.02±0.01	67±16
m2 (155 m)	0.06±0.01	50±8
m3 (153 m)	0.28±0.01	144±3
m4 (165 m)	0.06±0.01	26±7

Table 3: Phase difference, phase speed and wavelength between the m4, ww1 and m3 moorings at 153-165 m depth for the K1 tidal variability in temperature. The distance between m4 and ww1, and between m3 and ww1 are 13.25 and 13.69 km, respectively.

Mooring pair	Delta Phase [°]	Phase speed [m s^{-1}]	Wavelength (km)
ww1 – m4	50.1±7.2	1.1±0.2	95±15
m3 –ww1	67.8±3.8	0.8±0.05	73±4

Finally, we examine the spatial variability of horizontal tidal currents at diurnal frequency. For moorings m1 and m2, the tidal currents measured by the ADCPs and estimated by the harmonic analysis are weak, with amplitudes of less than 6 cm s^{-1} for m2 and less than 4 cm s^{-1} for m1. In addition, there is no apparent depth amplification of the tidal currents.

The results of the harmonic analysis for the currents measured by all ADCPs (except m1) are shown for K1 in Figure 16. The subsurface amplification of the currents is evident at the shallower moorings with speeds reaching 12.4 cm $s^{-1}$for ww1, 10.6 cm s^{-1} for m3 and 8.6 cm s^{-1} for m4. The maximum velocity is at 130-150 m depth for ww1 and m4, while it is shallower for m3 (70-110 m). The diurnal currents rotate with time in the CW direction at all moorings above 160-180 m. Below this depth, the currents are CCW. More specifically, the minimum of the m4 minor axis is at 178 m, deeper than that observed for ww1 (167 m). Above 100 m, the rotation coefficient for all moorings is close to one, corresponding to elliptical orbits with low eccentricity. Near 160-180 m, the K1 flows at ww1 and m4 are rectilinear. The angle of flow direction at zero Greenwich phase increases with depth for essentially all moorings, corresponding to downward phase and upward energy propagations. Between 100 m and 180 m, it is in ascending order for m4, ww1, and m3. This suggests that the phase propagation from m4 to ww1 and from ww1 to m3 is essentially northwestward, more or less along the shelf. The maximum phase difference between ww1 and m4, and between m3 and ww1 is ~ 30-40°, which is somewhat lower than the value found for temperature (close to 50-70°, see Table 3).

The K1 tidal currents are also shown geographically in Figure 17 in the form of ellipses for three depth intervals (98-100 m, 130-150 m, and ~180 m). The diurnal tidal flow is trapped at the shelf break and slope. The northwestward phase and energy propagation of the K1 signal previously estimated with the baroclinic energy flux calculations at ww1 and the temperature phase differences at ww1, m3 and m4, is qualitatively confirmed near 100 m and 140 m depth as the lines drawn in the ellipses rotate in the opposite direction (CCW) with respect to the currents (CW).

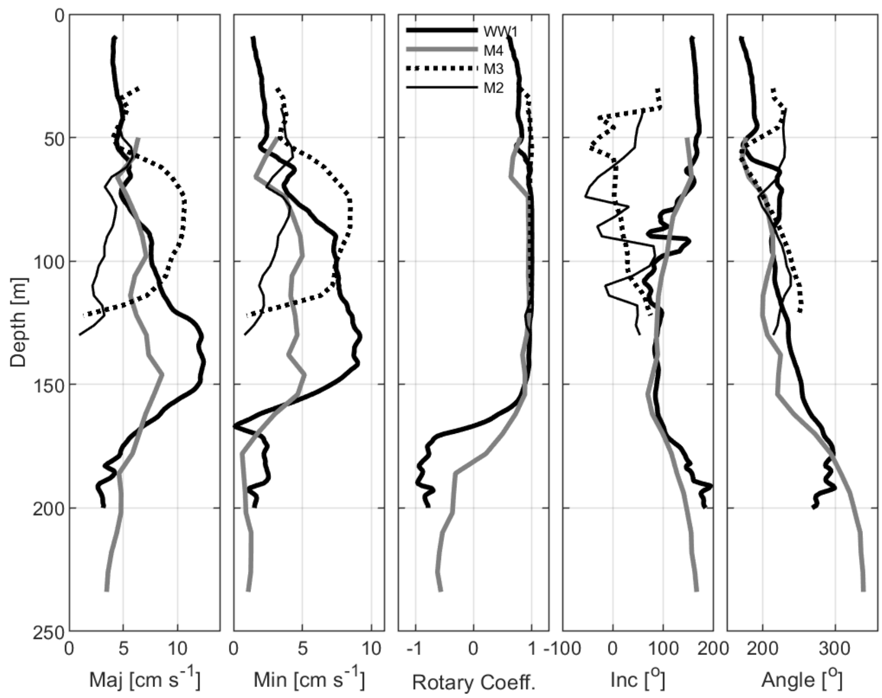

Figure 16: Results of the harmonic analysis applied to the currents measured by the ADCPs on ww1 (thick black), m4 (grey), m3 (dotted) and m2 (thin black). Vertical profiles of the K1 amplitude of major and minor semi-axes, the rotary coefficient, the ellipse inclination and the angle of the velocity vector at zero Greenwich phase.

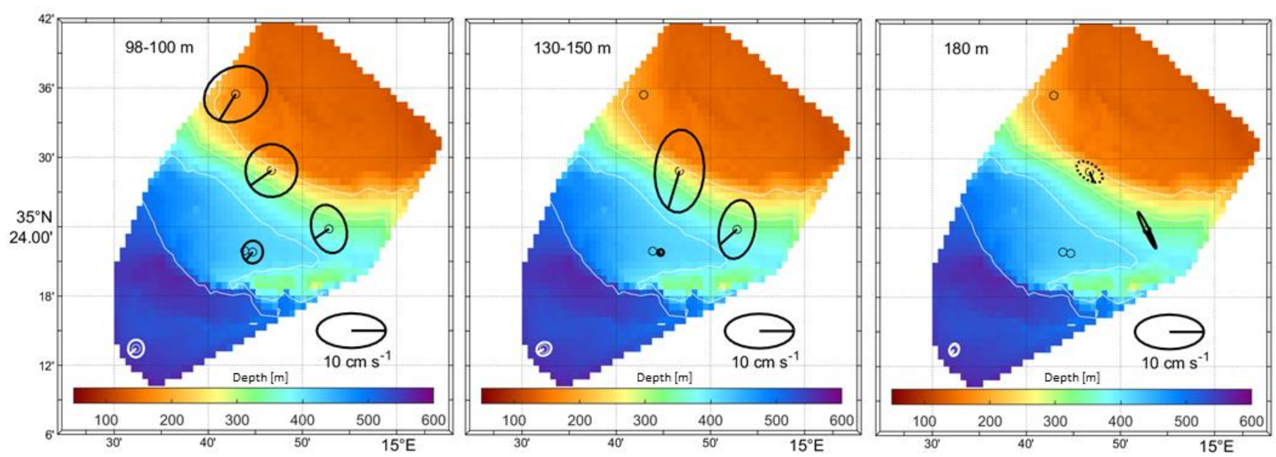

Figure 17: K1 tidal ellipses at the ADCP moorings near 100 m (left), 140 m (middle) and 180 m (right). Currents rotate in the CW (solid ellipse) and CCW (dotted ellipse) directions. The line in each ellipse represents the direction of the current at zero Greenwich phase. Bathymetry is shown with colors in the background (in m).

4 Discussion and conclusions

The tidal dynamics southeast of Malta in the central Mediterranean Sea were studied using measurements of temperature, salinity, and currents at several moorings in October and November 2020. In this area, numerical models of barotropic tides show the dominance of semi-diurnal (M2) oscillations of sea level with amplitude close to 10 cm. In contrast, the modeled barotropic currents are mainly diurnal (K1) with a maximum velocity of ~5 cm s^{-1}. The diurnal variability of the depth-averaged currents was confirmed by the data collected with the profiling ACDP at mooring ww1, although the models tend to underestimate their amplitude (Figure 9).

Our new Wirewalker observations show intense, mainly diurnal, vertical oscillations of the isotherms, isohalines and isopycnals (Figures 3 and 4), reaching an amplitude of 15-25 m near 160 m depth on the shelf break (for ww1). The corresponding vertical velocities are 0.1-0.2 cm s^{-1}.

The horizontal currents measured by ww1 show maximum variability in the surface mixed layer (above 60 m), mainly due to mesoscale and sub-mesoscale dynamics, and possibly inertial motions (Figure 5). Deeper in the water column (below 80 m), they are dominated by oscillatory signals that are enhanced near the shelf break. The most striking feature in the observations is the internal amplification of tidal diurnal currents below the seasonal thermocline (below 60 m depth). At the shelf break and slope (at moorings ww1 and m4), the diurnal currents are maximum with a velocity of 10-15 cm s^{-1} near 140 m depth, and are characterized by a minimum in the zonal direction (Figure 12), and in the amplitude of the semi-minor axis (Figures 13 and 16) near 170 m. Below this depth, they increase again with depth (more markedly for mooring ww1). The horizontal velocity minimum corresponds approximately to the maximum vertical displacement (~13 m) and the maximum vertical velocity (~0.1 cm s^{-1}) of the isopycnals (Figure 11).

Even though the time series are relatively short, there is an indication that the vertical (Figure 4) and horizontal (Figure 6) tidal currents at ww1 are fortnightly modulated, with maximum amplitude at the beginning and end of the study period and a minimum around 31 October corresponding to the spring tide (maximum sea level height, Figure 9). The zonal currents are either in phase (above 160-170 m) or out of phase (below 160-170 m) with the vertical isopycnal displacements (Figure 6), *i.e.*, in approximate quadrature with the vertical velocity (Figures 11 and 12). As a result, the K1 tidal flow appears as a normal mode-1 structure in the vertical and zonal directions (see Leblond and Mysak, 1978).

The separation of ww1 currents into barotropic (depth-averaged) and baroclinic components did not help to characterize the K1 internal flow. The modal decomposition in the zonal direction is less obvious, and the phase change near 160 m is only ~100° (compare the right and left panels in Figure 12). Moreover, the baroclinic flows above and below 160-170 m retain the same sense of rotation (CW) (see Figures 13 and 14). Baroclinic bandpass filtered pressure and velocity were combined to estimate the horizontal baroclinic energy flux associated with the internal tide at ww1. It was found to be bottom-intensified towards the west-northwest direction.

In summary, the observed diurnal (K1) internal tidal signal has the characteristics of an internal (or Kelvin-like) shelf wave propagating with the shelf (coast) on the right (*e.g.*, northwestward in our case). This wave is clearly seen in the zonal ww1 component of the velocities with a minimum near 160 m (Figure 12), and in the tidal ellipses with a minimum in the semi-minor axis and a change in rotation from CW (top) to CCW (bottom) (see Figures 13, 14, and 16).

The downward propagation of phase is ubiquitous in all results. It corresponds to an upward propagation of the group velocity and energy flux (Le Blond and Mysak, 1978). It is suggested that this may be an indication that part of the internal tide is generated by the local slope of the seafloor. The typical phase change is 1-2 °/m, which corresponds to a vertical wavelength of ~200-300 m.

Given the phase variations with depth, there are potential difficulties with evaluating the horizontal propagation using data at slightly different depths, and only qualitative results can be inferred. Analysis of the temperature variations at all moorings between 153 m and 176 m (Figure 15 and Table 2) shows the enhancement of the diurnal signal at the shelf break (mainly at ww1) and on the shelf (mooring m3). The difference between the phases of the K1 signal at the moorings, especially between m4, ww1, and m3 (Tables 2 and 3), shows a phase propagation toward the northwest with a phase velocity close to 1 m s^{-1}. The corresponding wavelength is of the order of 100 km. These values are similar to those calculated for diurnal internal tides near continental shelves elsewhere, for instance by Guo *et al*. (2012) in the South China Sea. The northwestward phase propagation, approximately along-shelf, is in good agreement with the direction of the baroclinic energy flux.

If vertical normal modes are calculated using the N^2 profiles shown in Figure 2 (Early *et al*., 2020) the first mode has a phase speed near 1 m s^{-1} with a maximal vertical velocity at 80-100 m depth, whereas our observations indicate a maximum much deeper at about 160 m (Figure 11). This is an indication of geometric differences between CTW modes subject to numerous boundary conditions (*e.g.,* Brink, 2006) and internal wave flat-bottom baroclinic normal modes.

The geographic variations of the K1 tidal currents (Figures 16 and 17) confirm the increase in subsurface velocities on the shelf and shelf break with tidal ellipse semi-axes approaching 10 cm s^{-1}. The phase differences of these currents are qualitatively consistent with the shelf wave propagation mentioned above.

The diurnal oscillations of the MLD (corresponding to the maximum in temperature diurnal signal near 60 m depth shown in Figure 9) can be compared to the findings of Artale *et al*. (1985) and Drago (1995) on the Adventure Bank and northwest of Malta, respectively. However, in our case the diurnal internal wave dominates much deeper below the sharp thermocline. At the thermocline, vertical displacements have an amplitude of only ~2 m (compared to 4-5 m for the previous studies mentioned above) and reach much larger values deeper near 160 m (> 10 m).

Despite the fact that the observations provide new and unique information about the internal tidal flow southwest of Malta in the central Mediterranean Sea, some of the results still remain not fully explained, and the theory of internal waves can be applied with some difficulty to determine the local tidal kinematics. In our data set, it is possible that the baroclinic K1 waves were generated at the Malta escarpment, a sharp meridional shelf slope to the northeast of our experiment site, and propagated to the mooring locations. There is also the possibility that the curved shelf edge causes a spatially-varying forcing of upslope currents that can resonantly and efficiently force a moving baroclinic wave, a process described for non-trapped semidiurnal internal waves by Zhang *et al.* (2014).

The convex form of the shelf edge around which the diurnal waves move, with the shelf on the right, differs in detail from the complicated bathymetry near Japan where diurnal waves were recently studied computationally by Nagai and Hibiya (2022), but there are enough similarities for that study to provide insight. In that paper, numerically modeled edge/bottom trapped diurnal waves were described as a sum of CTW modes. Interestingly, even with full 4D sampling of the waves in the model, they were still not able to describe the propagation and kinematics of the waves in complete detail. That result illustrates that the data from our few stations over a week may simply not be enough to fully describe the diurnal waves southeast of Malta. Note also that the phase propagation of a single traveling wave with a known dispersion relation gives information about group speed and energy flux, but this is not always true for a sum of waves. Many more than a few stations would be needed to properly perform a modal decomposition of the wavefield. So our alongshore wavelength and phase speed calculation has large error bars which would decrease with increased energy fraction in the dominant wave. The vertical phase propagation of our measured waves may be consistent with a modal sum, with the seabed-forced CTW energy spread among modes.

Numerical simulations, with or without assimilation of these observations, are necessary to further examine some of the results presented in this study, as demonstrated by the recent study just mentioned (Nagai and Hibiya, 2022). This is because the forcing of slowly propagating baroclinic waves by the action of much faster barotropic waves at a slope is subject, in general, to near-resonant effects or cancellation effects caused by the propagation (Zhang *et al*., 2014), with one example situation of a convex shelf edge mentioned above. These effects may be unique to specific locations and the particularities of seabed geometry, and numerical simulations are a reasonable tool to use to gain further understanding.

Acknowledgments

We thank Richard Stoner, Marina Ampolo-Rella, and Alessandro Brogini and the crew of the NATO Research Vessel Alliance for deploying and recovering the moorings during the MREP20 sea trial. Spectral and harmonic analyses were performed using the jLab data analysis package for Matlab, v.1.7.1, doi:10.5281/zenodo.4547006 (http://www.jmlilly.net/software) and the t_tide Matlab algorithm (https://www.eoas.ubc.ca/~rich/t_tide/t_tide_v1.3beta.zip).

We gratefully acknowledge NATO Allied Command Transformation Future Solutions Branch for supporting financially this study and the anonymous reviewers for constructive comments on the original manuscript.

References

Abdennadher, J., Boukthir, M., 2006. Numerical simulation of the barotropic tides in the Tunisian Shelf and the Strait of Sicily. J. Marine Syst., 63, 3-4, 162-182.

Abdennadher, J., Boukthir, M., 2016. Numerical study of the spatial distribution of the M2 internal tides in the Strait of Sicily. Geophys. Astro. Fluid., 110, 2, 111-129.

Artale, V., Provenzale, A., Santoleri, R., 1989. Analysis of internal temperature oscillations of tidal period on the Sicilian continental shelf. Cont. Shelf Res., 9(10), 867-888.

Brickman, D., Loder, J.W., 1993. Energetics of the internal tide on Northern Georges Bank. J. Phys. Oceanogr., 23, 409-424.

Brink, K.H., 2006. Coastal-trapped waves with finite bottom friction. Dyn. Atmos. Oceans, 41, 172-190.

Carrere, L., Lyard, F., Cancet, M., Guillot, A., 2015. FES 2014, a new tidal model on the global ocean with enhanced accuracy in shallow seas and in the Arctic region. In EGU general assembly conference abstracts (p. 5481).

Cosoli, S., Drago, A., Ciracolo, G., Capodici, F., 2015. Tidal currents in the Malta-Sicily Channel from high-frequency radar observations. Cont. Shelf Res., 109, 10-23.

Drago, A., 1995. Development of a capability in physical oceanography for the Maltese islands, M.Phil. Upgrading Report, Dept. of Oceanography, University of Southampton, U.K., p. 68.

Duda, T. F., Rainville, L., 2008. Dirunal and semidiurnal internal tide energy flux at a continental slope in the South China Sea. J. Geophys. Res., 113, C03025, doi: 10.1029/2007JC004418.

Early, J. J., Lelong, M. P., Smith, K. S., 2020. Fast and accurate computation of vertical modes. J. Adv. Model., 12, e2019MS001939, doi: 10.1029/2019MS001939

Feistel, R., 2012. TEOS-10: A new international oceanographic standard for seawater, ice, fluid water and humid air. Int. J. Thermophys, 33, 1335-1351.

Gasparini, G.P., Smeed, D.A., Alderson, S., Sparnocchia, S., Vetrano, A., Mazzola, S., 2004. Tidal and subtidal currents in the Strait of Sicily. J. Geophys. Res., 109, C02011.

Grancini, G. P., Michelato, A., 1987. Current structure and variability in the Strait of Sicily and adjacent area. Ann. Geophys, 5B(1), 75-88.

Guo, P., Fang, W., Liu, C., Qiu, F., 2012. Seasonal characteristics of internal tides on the continental shelf in the northern South China Sea., J. Geophys. Res., 117, C04023.

Huthnance, J.M., 1978. On coastal trapped waves: analysis and numerical calculation by inverse iteration. J. Phys. Oceanogr., 8, 74-92.

Le Blond, P.H., Mysak, L.A., 1978. Waves in the Ocean. Elsevier Oceanography Series 20. Elsevier Scientific Publishing Company, Amsterdam. 602 pp.

Molines, J. M., 1991. Modelling the barotropic tides in the Strait of Sicily and Tunisian shelf. Ocean. Acta, 14, 241-252.

Mysak, L.A., 1980. Recent advances in shelf wave dynamics. Rev. Geophys. Space Phys., 18(1), 211-241.

Nagai, T., Hibiya, T., 2022. Diurnal coastal trapped waves and associated deep-ocean mixing near the head of Suruga Trough. J. Geophys. Res., 127, e2022JC018457, doi: 10.1029/2022JC018457.

Nash, J., Alford, M. H., Kunze, E., 2005. Estimating internal wave energy fluxes in the ocean. J. Atmos. Ocean. Technol., 22, 1551-1570.

Padman L., Erofeeva, S. 2004. A barotropic inverse tidal model for the Arctic Ocean. Geophys. Res. Lett., 31(2), L02303, doi: 10.1029/2003GL019003.

Pawlowicz R., Beardsley B., Lentz S., 2002. Classical tidal harmonic analysis including error estimates in MATLAB® using T_TIDE, Comput. Geosci., 28, 929-937.

Pingree, R. D., Mardell, G. T., New, A. L., 1986. Propagation of internal tides from the upper slopes of the Bay of Biscay. Nature, 321, 154-158.

Pinkel, R., Goldin, M. A., Smith, J. A., Sun, O. M., Aja, A. A., Bui, M. N., Hughen, T. 2011. "The wirewalker: A vertically profiling instrument carrier powered by ocean waves." J. Atmos. Ocean. Technol., 28, 426-435.

Poulain, P.-M., Menna, M., Gerin, R., 2018. Mapping Mediterranean tidal currents with surface drifters. Deep-Sea Res. Part I, 138, 22-33.

Poulain, P.-M., Stoner, R., Lewis, C. Ampolo-Rella, M., Cozzani, E., 2019. Testing the wirewalker profiling system for high-frequency underwater dynamics characterization. CMRE Memorandum Report CMRE-MR-2019-22, La Spezia, Italy. 32 p.

Poulain, P.-M., Oddo, P., 2020. Cruise report and datasets collected during the MREP20 sea trial. CMRE Technical Progress Report A06.4.2.1, CMRE, La Spezia, Italy. 29 p.

Pugh, D.T., 1987. Tides, Surges and mean sea level. John Wiley and Sons, New York, 472 p.

Ray, R. D., Mitchum, G.T, 1997. Surface manifestation of internal tides in the deep ocean: observations from altimetry and island gauges. Prog. Oceanogr., 40(1-4), 135-162.

St. Laurent, L., Garrett, C., 2002. The role of internal tides in mixing the deep ocean. J. Phys. Oceanogr. , 32, 2882-2899.

Tsimplis, M.N., Proctor, R., Flather, R.A., 1995. A two-dimensional tidal model for the Mediterranean Sea. J. Geophys. Res. Oceans, 100, C8, 16,223-16,239.

Visbeck, M., 2002. Deep velocity profiling using lowered acoustic Doppler current profilers: Bottom track and inverse solutions. J. Atmos. Ocean. Technol., 19(5), 794-807.

Waterhouse, A.F, Mackinnon, J.A., Musgrave, R.C., Kelly, S.M., Pickering, A., Nash, J., 2017. Inerntide convergence and mixin in a submarine canyon. J. Phys. Oceanogr., 47, 303-322, doi: 10.1175/JPO-D-16-0073.1

Wunsch, C., 1975. Internal tides in the ocean. Rev. Geophys., 13(1), 167-182.

Zhang, W.G., Duda, T.F., Udovydchenkov, I.A., 2014. Modeling and analysis of internal-tide generation and beamlike onshore propagation in the vicinity of shelfbreak canyons. J. Phys. Oceanogr., 44(3), 834-849.

Appendices

A) Fluctuations of the RBR and SBE sensor depth

Analysis of the pressure measured by the RBR and SBE sensors on the moorings revealed that a semi-diurnal signal with an amplitude of 0.2 dbar is predominant. The phase of this signal is identical for all moorings. Moreover, the amplitude and phase agree quite well with the values predicted by the OSU TPXO barotropic tidal model (Padman and Erofeeva, 2004). Figure A1 shows an example for the RBR sensors on mooring m3. The increase in the magnitude of the oscillation with decreasing depth is due to the additional contribution resulting from the motion and tilt of the mooring line. Indeed, the diurnal currents induce semi-diurnal fluctuations in the inclination, hence semi-diurnal variations in sensor depth. In addition to the semi-diurnal variations, there are some intermittent events at moorings m3 and m4 with depth residuals up to 1.5 m, which are likely caused by mooring line motion since they coincide with enhanced barotropic flows measured by the ADCP.

Let us assess the effects of sensor depth variations on measurements, such as temperature. Consider the mean temperature profile obtained with ww1 (see Figure 2). In the thermocline and below 80 m depth, the gradient is about 0.05 and 0.03 °C m^{-1}, respectively. Thus, a peak-to-peak depth change of 0.4 m results in a temperature change of ~0.01 °C. For extreme events with a peak-to-peak variation of 3 m, the effect on temperature is less than 0.15 °C. We therefore conclude that the depth variations of the sensors at the mooring are not significant and that the constant depth approximation is valid.

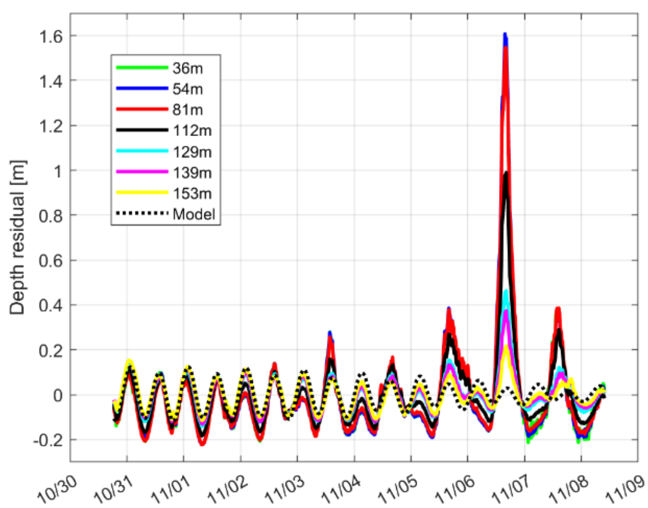

Figure A1: Depth residuals at the RBR sensors on the m3 mooring versus time, along with sea surface elevation predicted by the OSU TPXO barotropic tide model.

B) Estimation of the high-frequency isopycnal vertical displacement

High-frequency (mostly tidal) vertical displacements of the isopycnals were estimated by automatically comparing individual potential density anomaly profiles with their 3-day running mean values. For a given density value in the individual profile, the same value was sought in the mean profile. If it was found, the vertical distance between the two values was considered as an estimate of the vertical displacement and assigned to the depth of the mean value. Figure B1 shows an example of two profiles near the beginning of the observational period. The low-pass filtered profiles at the times of the individual profiles are approximately the same. Vertical displacements are indicated by arrows for depths near 65 m and 170 m. This method does not work in the surface mixed layer, where density is homogeneous, and below 180 m, because the deepening of the isopycnal exceeds the maximum ww1 depth (it is between 200 m and the bottom depth of 220 m). Note that for the example shown in Figure B1, the vertical displacements are minimum (close to zero) near 90 m depth.

The method described above was compared to the method based on temperature gradients (*e.g.*, Brickman and Loder, 1993; Duda and Rainville, 2008). If temperature is separated in its temporal mean ($\bar{T}$) and anomaly (T') such that T(z,t) = $\overline{T}$ (z) + T'(z,t), the vertical velocity W can be estimated as follows:

$$W = - \partial T'/\partial t \;/\; \partial \overline{T}/\partial z \,.$$

Our method provided a similar result, but with better accuracy, since the division of terms in the above equation can introduce large errors.

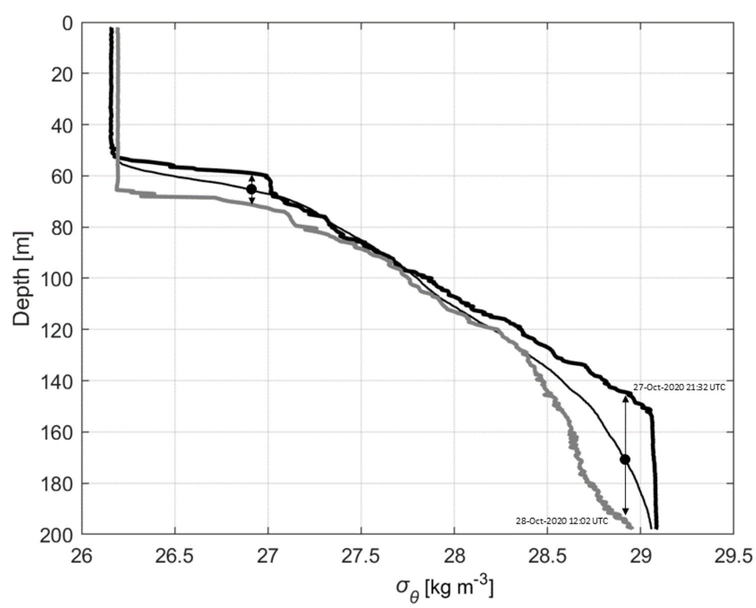

Figure B1: Potential density anomaly profiles on 27 October at 21:32 UTC (dark gray) and 28 October at 12:02 UTC (light gray) and corresponding lowpass-filtered profiles. Vertical isopycnal displacements are shown with arrows near depths of 65 m and 170 m.

C) Contamination by inertial signals

At the latitude of ww1 (35°N 28.86’) the inertial (20.67 h) and K1 tidal (23.93 h) periods are close to each other, and long time series are required to separate inertial and diurnal signals. To evaluate the possible contamination of the diurnal tide magnitude by inertial oscillations, we have fitted clockwise motions to the currents measured by the ww1 ADCP at both the inertial and K1 frequencies. The results are shown in Figure C1. The dominance of K1 tidal currents compared to the inertial signals is striking above 170 m depth. In particular, the inertial currents are limited to 3 cm s^{-1} (corresponding to less than 5% of the velocity variance) while tidal currents can exceed 10 cm s^{-1}, with an explained variance exceeding 50%.

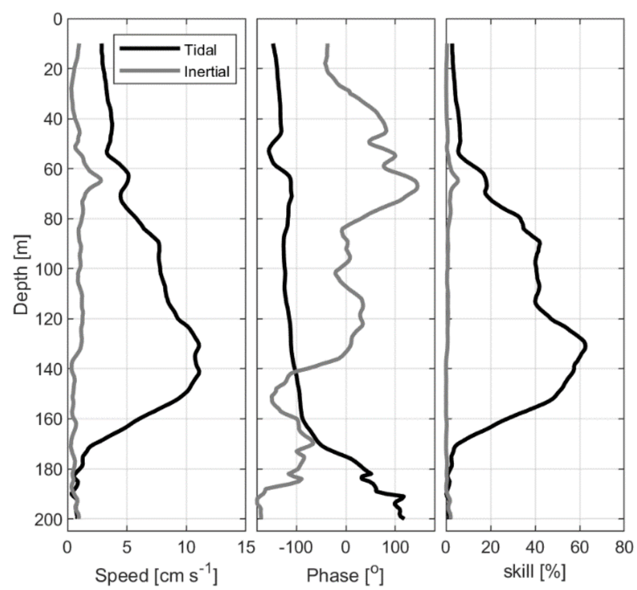

Figure C1: Least squares fit of clockwise motion at inertial (gray) and K1 tidal (black) frequencies applied to the ww1 ADCP currents for the period 27 October – 8 November 2020.